SELECTION OF A DYNAMICALLY SCALED LIFT AND THRUST-COMPOUNDED HELICOPTER CONFIGURATION: KEY INSIGHTS FROM MACH-SCALED WIND TUNNEL TESTING

Vivek Uppoor
Graduate Research Assistant

Inderjit Chopra
Distinguished University Professor & Director

Alfred Gessow Rotorcraft Center
University of Maryland
College Park, MD, USA

ABSTRACT

This paper presents a high-speed wind tunnel investigation of compound helicopter aeromechanics, focusing on the effects of various lift and thrust compounding strategies. Six rotorcraft configurations, incorporating various combinations of wings and a pusher propeller, were tested at advance ratios up to 0.7. The comprehensive dataset includes measurements of performance, blade structural loads, and hub vibratory loads. The test data were used to validate the University of Maryland Advanced Rotorcraft Code (UMARC) comprehensive analysis model. Results show that asymmetric half-wing lift compounding is most beneficial for maximizing high-speed lift-to-drag ratio due to a combination of wing-rotor lift sharing and rotor lift offset. Wing lift sharing significantly reduces blade structural and vibratory loads. At high advance ratios, achieving propulsive trim requires substantial propeller power, exceeding that of the main rotor. The objective of this research is to gain insight into the features of compound helicopters that enable efficient high-speed flight to inform future design decisions.

NOTATION

Symbols

A	Rotor disk area, πR^2, ft^2
A_T	Tunnel cross-sectional area, ft^2
A_W	Half-wing area, ft^2
C_{D_W}	Wing drag coefficient, $D_W/\rho A(\Omega R)^2$
C_H	Horizontal longitudinal force coefficient, $H/\rho A(\Omega R)^2$
C_L	Lift coefficient, $L/\rho A(\Omega R)^2$
C_{L_W}	Wing lift coefficient, $L_W/\rho A(\Omega R)^2$
C_{M_X}	Hub rolling moment coefficient, $M_X/\rho A(\Omega R)^2 R$
C_{M_W}	Wing rolling moment coefficient, $M_W/\rho A(\Omega R)^2 R$
C_Q	Torque coefficient, $Q/\rho A(\Omega R)^2 R$
C_T	Thrust coefficient, $T/\rho A(\Omega R)^2$
C_X	Propulsive force coefficient, $X/\rho A(\Omega R)^2$
C_W	Wing download coefficient, $W/\rho A(\Omega R)^2$
D_W	Wing drag force, positive rearward, lb
FM	Figure of Merit
F_X, H	Rotor horizontal force in hub frame, positive aft, lb
F_Z, T	Rotor vertical force in hub frame, positive up, lb
F_{XY}	Total hub in-plane force, lb
L	Lift force, lb
L_W	Wing lift force, lb
L/D	Aircraft lift-to-drag ratio
L/D_e	Rotor effective lift-to-drag ratio
LO	Lift offset, C_{M_X}/C_T, % R
M_{tip}	Hover tip Mach number, $\Omega R/a$
M_W	Wing rolling moment, positive roll right, in-lb
M_X	Hub rolling moment, positive roll right, in-lb
M_Y	Hub pitching moment, positive nose up, in-lb
Q	Rotor torque, positive opposite to rotor rotation, in-lb
R	Rotor radius, ft
V_∞	Wind tunnel speed or freestream speed, ft/s
X	Propulsive force, positive forward, lb
α_s	Shaft tilt angle, positive rearward, degree
η_p	Propulsive efficiency
θ_{1c}, θ_{1s}	Lateral and longitudinal cyclic angles, degree
θ_{75}	Collective blade pitch angle at 75% radial station, degree
θ_w	Wing incidence relative to freestream, degree
λ_c	Propeller cruise inflow
μ	Advance ratio, $V_\infty/\Omega R$
ρ	Air density, slug/ft^3
σ	Rotor solidity, $N_b c/\pi R$
ψ	Rotor azimuth angle, degree
Ω	Rotor rotation speed, rad/s

Acronyms

MFW	Maryland Free Wake
RPM	Revolutions Per Minute

Presented at the 51st European Rotorcraft Forum, Venice, Italy, 9–11 September, 2025.

SMR Single Main Rotor
TURNS Transonic Unsteady Rotor Navier Stokes
UMARC University of Maryland Advanced Rotorcraft Code

INTRODUCTION

High-speed variable-RPM edgewise rotorcraft represent an emerging frontier in vertical flight, demanding integrated advancement in rotor aeromechanics, propulsion, and configuration design beyond conventional platforms. To exceed the single main rotor (SMR) helicopter's 170-knot barrier, novel configurations must overcome the aerodynamic penalties imposed on the main rotor at high speeds, while preserving the efficient hover performance and low-speed agility central to traditional helicopters. A large-diameter rotor, optimized for efficient hover, quickly becomes a liability in high-speed flight. Advancing blade compressibility effects, large reverse flow regions, and dynamic stall on the retreating side severely reduce performance while causing significant structural and vibratory loads (Refs. 1, 2). At high advance ratios, these aerodynamic extremes are accompanied by competing control demands: the rotor must simultaneously generate substantial forward thrust and correct for rotor lift dissymmetry.

Compound rotorcraft address the conflicting demands of high-speed and hovering flight by redistributing lift and thrust from the rotor across multiple components. To reach high speeds, helicopters must first overcome advancing blade tip compressibility, which is addressed by reducing rotor speed at the cost of operation at high advance ratios. In this regime, lift compounding with auxiliary wings offloads the rotor, reducing blade loading and limiting the negative effects of the expanded reverse flow region on the retreating side. Asymmetric lift compounding, achieved by using a wing solely on the retreating side, mitigates high-μ rotor airflow dissymmetry by introducing lift offset. This shifts the stiff rotor's net lift vector toward the advancing side, where dynamic pressure is higher, and generates an aerodynamic rolling moment (M_X) on the airframe (Ref. 3). The asymmetric half wing opposes the rolling moment from the rotor (M_W). This is represented in Figure 1. Lift offset is defined in Equation 1.

$$\text{LO}\ (\%R) = \frac{C_{M_X}}{C_T} = \frac{-C_{M_W}}{C_T} \tag{1}$$

Thrust compounding extends the operational envelope by supplementing the slowed rotor with an independent source of

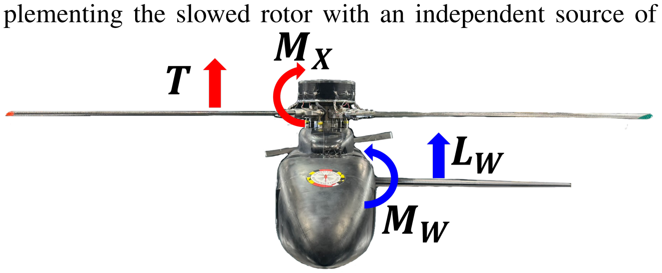

Figure 1. Diagram of lift offset for a half-wing compound rotorcraft with a hingeless rotor hub.

axial thrust, commonly a pusher propeller. Decoupling lift and thrust production enables the rotor to operate at any shaft angle, reducing aerodynamic penalties from forward rotor tilt and fuselage form drag. At high speeds, the rotor may be tilted rearward into a partial descent state, decreasing required torque (Refs. 4, 5).

Interest in compound rotorcraft surged in the mid-20th century, with a series of full-scale experimental programs exploring a wide range of configurations, including the tip-jet driven Fairey Rotodyne and McDonnell XV-1 helicopter-autogyro hybrids, the coaxial Sikorsky XH-59, and the modular S-72 Rotor Systems Research Aircraft (RSRA) (Refs. 6–9). These efforts demonstrated the feasibility and performance benefits of compound designs for high-speed flight but were ultimately constrained by structural dynamics and propulsion limitations, particularly high vibratory loads and the lack of variable-speed rotor systems. The Lockheed XH-51A demonstrated high-speed flight up to 263 knots ($\mu = 0.72$), but rotor speed could not be reduced below 95% nominal due to the onset of structural resonance (Refs. 10–12). Advancements in modern composite materials, digital control systems, and the innovation of variable RPM engines that facilitate slowed rotors (Ref. 13) have sparked renewed interest in compound rotorcraft (Ref. 14). The Piasecki X-49A SpeedHawk features a wing for lift-sharing and a vectored thrust ducted propeller integrated propulsion/anti-torque system for use in both forward flight and hover. Similarly, the lift and thrust-compounded Airbus X^3 is equipped with two wing-mounted propellers used for auxiliary propulsion in cruise and anti-torque in hover (Ref. 15). The X^3 is succeeded by the Airbus RACER, demonstrating improved performance at $\mu > 0.6$ (Ref. 16). Bell has developed the lift-compounded 360 Invictus with detachable wings, enabling mission-dependent selection between high-speed flight and enhanced hover performance. Sikorsky's thrust-compounded X2 Technology™ Demonstrator and its successor, the S-97 Raider, employ stiff coaxial rotors with lift offset (advancing blade concept) to mitigate high advance ratio lift degradation without relying on wing offloading, enabling high-speed flight while preserving hover performance (Ref. 17). The X2 Technology™ Demonstrator achieved 250 kt flight at $\mu = 0.8$ using a pusher propeller (Ref. 18).

These development programs employ diverse compounding methodologies to achieve high-speed flight; however, consensus on an optimal configuration has yet to emerge. Each approach involves trade-offs in performance, structural loads, vibration, vehicle complexity, and mission adaptability. Hence, the extensive compound rotorcraft design space requires a detailed parametric exploration of vehicle configurations. Several studies have employed analytical tools such as the University of Maryland Advanced Rotorcraft Code (UMARC), the Comprehensive Analytical Model of Rotorcraft Aerodynamics and Dynamics II (CAMRAD II), and the Rotorcraft Comprehensive Analysis System (RCAS) to model compound rotorcraft configurations (Refs. 19–23). Sugawara et al. have used high-fidelity computational fluid dynamics (CFD) tools to investigate the impact of lift-share ratio on a

UH-60-based winged compound helicopter (Ref. 24). Frey et al. have coupled CFD and comprehensive analysis to study aerodynamic interactions among the main rotor, wing, and propeller on the Airbus RACER in hover and cruise flight (Refs. 25, 26). Despite the abundance of analytical studies, experimental validation remains scarce. In his Nikolsky Lecture, Ormiston highlighted the critical role of systematic wind tunnel testing in advancing the development of high-speed compound rotorcraft and in validating comprehensive analysis models (Ref. 14). Boeing has conducted wind tunnel tests on a 30%-scaled AH-64E configured for lift and thrust compounding at the Boeing V/STOL Wind Tunnel (BVWT) (Ref. 27). Sikorsky performed a wind tunnel test of a 1/5-scale thrust-compounded X2 Technology™ coaxial rotor and propeller system at the National Full Scale Aerodynamics Complex (NFAC) (Ref. 28). Test data from these wind tunnel entries are not available in the public domain.

In an effort to address the lack of experimental data, the University of Maryland (UMD) Alfred Gessow Rotorcraft Center has conducted systematic wind tunnel experiments in five phases, investigating the aeromechanics of lift and thrust-compounded rotorcraft to validate comprehensive analysis tools. Phase 1 focused on the behavior of hingeless slowed rotors at high advance ratios, establishing a baseline for comparison (Refs. 29, 30). Phases 2 and 3 introduced individual compound elements: an asymmetric half wing for lift compounding and a pusher propeller for thrust augmentation, respectively. These tests revealed performance gains and reduced vibratory loading through rotor-wing lift sharing and rearward shaft tilt (Refs. 4, 31). Phases 4 and 5 combined both compounding elements, testing the half-wing and full-wing lift and thrust-compounded configurations respectively (Refs. 5, 32, 33). Achieving a greater wing lift fraction was found to be essential for achieving efficient high-speed performance and reducing vibratory loads.

This study investigates the performance, blade structural loads, hub vibratory loads, and aerodynamic interactions of the entire range of compound configurations tested throughout this program. The resulting dataset provides a fundamental understanding of lift and thrust-compound rotorcraft aeromechanics, as well as some critical test-verified insights and configuration selection recommendations for vehicle designers.

Scope of Paper

The UMD compound helicopter test campaign has experimentally investigated the following slowed rotor compound rotorcraft configurations:

1. Isolated single main rotor (SMR).
2. Half wing lift compound. Wing area = A_w.
3. Full wing lift compound. Wing area = $2A_w$.
4. Pusher propeller thrust compound.
5. Half wing and pusher propeller lift and thrust compound. Wing area = A_w.
6. Full wing and pusher propeller lift and thrust compound. Wing area = $2A_w$.

(a) Thrust Compound

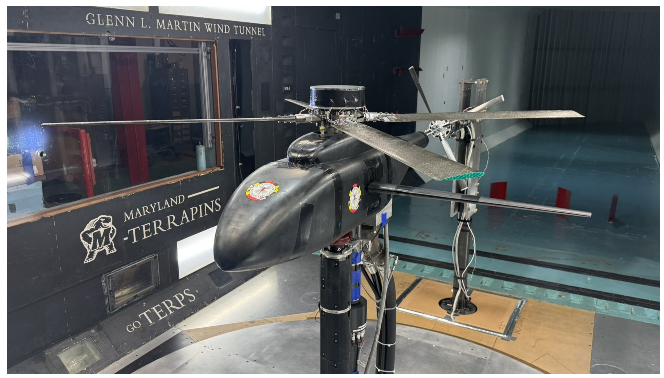

(b) Half-Wing Lift and Thrust Compound

(c) Full-Wing Lift and Thrust Compound

Figure 2. UMD compound rotorcraft configurations tested in the Glenn L. Martin Wind Tunnel.

Figure 2 shows configurations 4-6. The main rotor and fuselage are consistent between test configurations. The isolated slowed rotor configuration serves as the baseline for comparison.

This paper presents a comparative study of compound rotorcraft configurations. The first two sections describe the compound rotorcraft test model and the comprehensive analysis methodology. The third section examines hover testing of the lift-compounded configurations. The following three sections outline the wind tunnel test and examine specific results: lift compound results, lift and thrust compound results.

COMPOUND ROTORCRAFT MODEL

This study utilizes the UMD compound rotorcraft model, which comprises a lift-compounded helicopter test stand and a separate propeller stand.

Compound Rotor Rig: The UMD compound rotorcraft rig has a four-bladed, hingeless main rotor with rectangular composite blades having the NACA 0012 airfoil. The rotor has a 5.57 ft diameter with a 16.5% root cutout. The main rotor is operated at 700 RPM, corresponding to a hover tip Mach number of $M_{\text{tip}} = 0.18$; this is 30% of the Mach-scaled 2300 RPM. The rotor system is stiff at this operating speed, with the first flap frequency at 1.51/rev. The main rotor fan plot is shown in Figure 3. Full-bridge strain gages at 25%R on each blade measure flap, lag, and torsion moments in the rotating frame. A five-axis hub balance measures rotor loads in the nonrotating frame. Rotor torque is measured with strain gages mounted on the rotor shaft. A modified ROBIN fuselage, mounted at 0° shaft tilt, houses the hydraulic rotor drive system, 27V DC-motor actuators, swashplate, three-axis accelerometers, and hub balance. Each blade pitch grip uses a Hall Effect sensor to measure root blade pitch with a 0.3° accuracy.

Lift compounding is achieved with modular fixed wings. The wings can be attached to the retreating and advancing sides of the fuselage independently. Each half-wing spans 70% of the main rotor radius and features a linear taper ratio of 0.5, an aspect ratio of 5, and zero built-in twist. The section profile transitions from a NACA 0020 at the root to a NACA 0015 at the tip. Wings are mounted 24%R below the hub and centered longitudinally. Independent 5-component balances are integrated into each wing. Incidence angles can be set between 0° and 12°. This study investigates a fixed 8° wing incidence as high lift offloading has yielded improved performance and minimized rotor loads in previous studies (Refs. 5, 33).

Propeller Test Stand: The propeller thrust stand is included for thrust compounding. A trailing pusher propeller is mounted 1.3R aft of the main rotor. The propeller hub is centered with the fuselage tail boom. The propeller assembly is mounted separately from the compound rotor rig on the tunnel floor to eliminate vibratory load transmission. The composite 4-bladed propeller has a diameter of 26 inches, approximately 40% of the main rotor diameter. The uniform rectangular blades utilize a NACA 0012 airfoil and have a −40° linear spanwise twist. The collective pitch was set to 40°. A brushless DC motor powers the propeller. Hub loads are recorded in the nonrotating frame using an ATI-45 Mini 6-axis load cell.

This test model uniquely captures independent nonrotating frame loads at four locations: (1) 6-axis rotor hub loads, (2) 5-axis loads at the retreating side wing, (3) 5-axis loads at the advancing side wing, and (4) 6-axis propeller hub loads. This arrangement enables measurement of rotor-wing-propeller aerodynamic interactions.

The compound model properties are listed in Table 1.

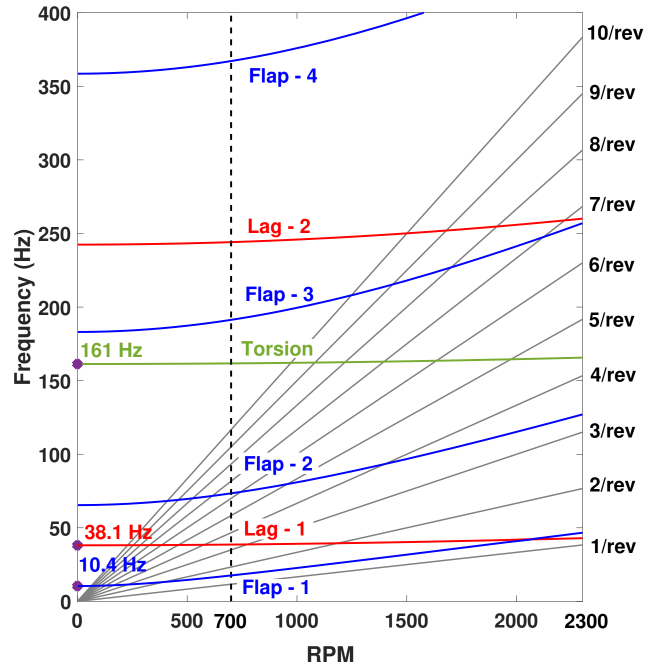

Figure 3. Fan plot of the hingeless main rotor with composite blades. At 700 RPM: 1st flap is 1.51/rev, 1st lag is 3.3/rev, and 1st torsion is 14.1/rev.

COMPREHENSIVE ANALYSIS

Analytical results were obtained using the University of Maryland Advanced Rotorcraft Code (UMARC). This code includes modules to include all components of a compound rotorcraft, including the main rotor, wings, and propeller (Ref. 34). Recent updates have been implemented to support independent retreating and advancing wing incidences. UMARC has been validated against wind tunnel test data of independent lift-compound and thrust-compound configurations (Refs. 4, 31) and of combined lift and thrust-compounded configurations (Refs. 5, 33).

Main Rotor Analysis

The main rotor blades are structurally modelled as elastic beams using the Hodges-Dowell theory, which includes up to second-order nonlinearities (Ref. 35). Flap, lag, torsion, and axial deformations are included. The blade dynamics were resolved using finite element analysis with 20 radial elements and 12 time steps per revolution. Third-order shape functions were applied to the flap, lag, and axial motions, while torsion was modeled using a quadratic shape function. Temporal elements used fifth-order polynomials.

The main rotor aerodynamic model uses unsteady lifting line theory with NACA 0012 C81 airfoil tables generated by the in-house CFD code TURNS (Transonic Unsteady Rotor Navier-Stokes) (Ref. 36). The rotor near-wake is modelled using the Weissinger-L near-wake representation with the wake trailing in-plane with the rotor for 30° in azimuth and skewed

Table 1. UMD Compound Rotorcraft Properties

Characteristic	English	Metric
Main Rotor		
Rotor Radius	2.79 ft	0.85 m
Chord	0.26 ft	0.08 m
Number of Blades	4	
Solidity	0.12	
Root Cutout Location	0.165 R	
Airfoil	NACA 0012	
Planform	Untwisted, Untapered	
Lock Number	4.75	
Operating RPM	700	
Tip Mach Number	0.18	
First Flap Frequency	1.51/rev	
First Lag Frequency	3.3/rev	
First Torsion Frequency	14.1/rev	
Propeller		
Radius	1.08 ft	0.33 m
Number of Blades	4	
Airfoil	NACA 0012	
Solidity	0.144	
Twist	-40°	
Pitch θ_{75}	40°	
Prop vertical position	0.24 R below hub	
Prop lateral position	1.3 R aft of hub	
Wing (one per side)		
Wingspan	1.95 ft	0.59 m
Chord (root, tip)	0.52, 0.26 ft	0.16, 0.08 m
Aspect Ratio	5	
Taper Ratio	0.5 (Linear)	
Wing airfoils (root, tip)	NACA 0020, NACA 0015	
Wing position (below hub)	0.24 R	
Wing longitudinal position	Centered with the hub	

with forward flight velocity (Ref. 37). The near wake is modeled by collapsing the horseshoe vortex circulation strength from 50 blade panels into five discrete vortex filaments. The far wake is modelled using the time-accurate Maryland Free Wake (MFW) model with 7.5° azimuthal spacing (Ref. 38). A single vortex trailer is released from each blade tip with circulation strength equal to the peak blade circulation outboard of 0.3R. Each filament has an initial core radius of 10% of the blade chord and uses a turbulent core growth model. The free wake model captures distortions from interactions with trailers from other lifting surfaces. The Leishman-Beddoes unsteady model is included to capture dynamic stall effects (Ref. 39).

Wing Analysis

The wing spar is constructed with steel and is assumed to be structurally rigid. The wing aerodynamic model uses lifting line theory. Each wing is divided into 50 spanwise segments, each represented by a bound horseshoe vortex with a free wake. The wake geometry is distorted using the time-accurate Maryland Free Wake model. The 2D airfoil tables for the NACA 0020 (wing root) and NACA 0015 (wing tip) were generated using TURNS CFD. Intermediate spanwise positions use linearly interpolated airfoil data from these tables. Induced velocity is calculated using the Weissinger-L methodology from the rotor, wing, and propeller trailers (Ref. 40).

Propeller Analysis

The composite propeller blades and aluminum hub are assumed to be structurally rigid. Propeller aerodynamics is included using a lifting-line approach with 50 spanwise panels per blade. The NACA 0012 airfoil tables were generated using the in-house 2D Hamiltonian Paths and Strands (HAM2D) CFD at the lower Reynolds numbers experienced by the propeller blades (Ref. 41). A single free tip trailer is released from each propeller blade with the same properties as the main rotor tip trailer. Trailer distortion and interactions with rotor and wing trailers are captured using the MFW.

HOVER TESTING

Compound rotorcraft hover performance is impacted by wing download from the rotor wake. Hence, hover testing was performed to measure the rotor-wing interactional effects on an elevated tower out of ground effect. Rotor loads were measured using the rotor hub balance and the wing download (C_W/σ) from rotor wake impingement was measured using the wing balances. Figure 4 shows the compound rotor rig mounted on the hover tower.

Figure 4. Compound rotor rig with the full wing configuration installed on the UMD hover tower.

The hover analysis was performed with UMARC, though the effects of wake blockage from the wings were added separately. The wake blockage effect cannot be modeled with the wing's lifting line-based wake model. Wing download due to rotor wake impingement was estimated by applying the induced velocities from the rotor's free wake at the wing plane, assuming a drag coefficient of $C_D = 1.28$, which corresponds to flow normal to a flat plate (Ref. 42). The induced velocities are assumed to be normal to the wing plane.

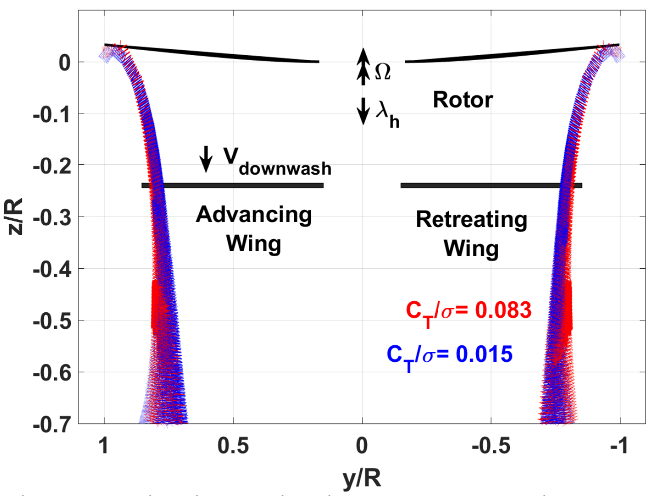

Figure 5. Wing immersion in rotor wake during hover. Wake boundary determined by the Maryland Free Wake.

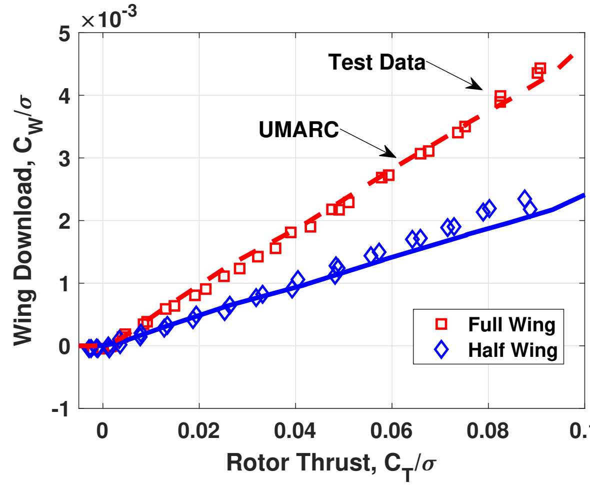

Figure 6. Hover download due to rotor wake impingement. Ω = 700 RPM.

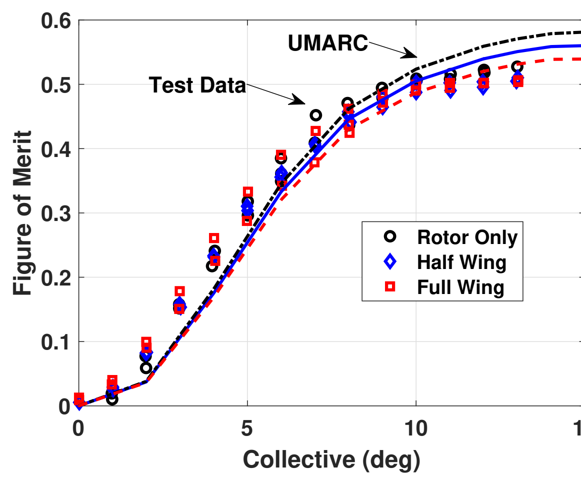

Figure 7. Net figure of merit. Ω = 700 RPM.

Figure 5 shows the free wake boundary in hover at two rotor thrust levels. Most of the wing area remains immersed in the rotor wake regardless of main rotor thrust. The wing's 0.5 taper ratio concentrates larger chord sections inboard and immersed in the downwash.

Figure 6 presents the measured wing download in hover resulting from rotor wake impingement. The half-wing and full-wing configurations experience download equivalent to approximately 2.5% and 5% of the rotor thrust, respectively. Predictions from UMARC show good agreement with the experimental measurements.

Relative hover performance between the isolated rotor and lift-compounded configurations is evaluated using the net figure of merit, as defined in Equation 2.

$$FM_{net} = \frac{(C_T - C_W)^{3/2}}{C_Q\sqrt{2}} \tag{2}$$

As shown in Figure 7, all configurations yield a similar FM at low collective pitch angles, where wing download is negligible. At a collective of 13°, the net figure of merit decreases by 4.5% from the isolated rotor configuration to the full-wing configuration due to increased wing download. The isolated rotor configuration yields a relatively poor figure of merit, attributed to its untwisted, rectangular planform and use of a symmetric airfoil.

WIND TUNNEL TESTING

Wind tunnel testing was performed at the closed-circuit Glenn L. Martin Wind Tunnel (GLMWT) at UMD. Figure 8 shows the test model mounted in the GLMWT in the full-wing and pusher propeller lift and thrust-compound configuration. The tunnel test section measures 7.75 ft in height and 11.04 ft in width. The rotor hub is positioned 5.9 ft above the tunnel floor and centered spanwise within the test section. The rotor-to-test-section area ratio is 0.29. Wall interference effects are estimated using the Prandtl–Glauert correction, expressed as $\Delta\alpha_s = \delta_w L/(qA_T)$ radians, with a correction coefficient $\delta_w = 0.12$ specific to the GLMWT. Wall boundary effects are minimal, as $\Delta\alpha_s \leq 0.25°$ for all test points at and above $\mu = 0.5$.

Lift compound wind tunnel trim is achieved using loads measured by the rotor balance and wing balances. The net lift target is reached by tuning the rotor collective. The net rolling and pitching moments about the rotor hub are trimmed to zero using the rotor cyclic control angles. Wing forces and moments are transformed to the body frame centered at the rotor hub. The trim error threshold was ±10 in-lb, corresponding to $C_{Mx}/\sigma, C_{My}/\sigma < \pm 0.001$. Lift and thrust compound wind tunnel trim involves the same trim methodology as the lift compound configuration, except that it includes fuselage drag and propeller thrust. Propulsive trim is reached by setting the propeller thrust equal to the fuselage, rotor, wing, and propeller drag. Blade tracking was verified using a strobe light reflecting off colored tape applied to each blade tip. Pitch link adjustments were made to maintain tracking within half of the blade thickness.

The wind tunnel test campaign explored a wide range of com-

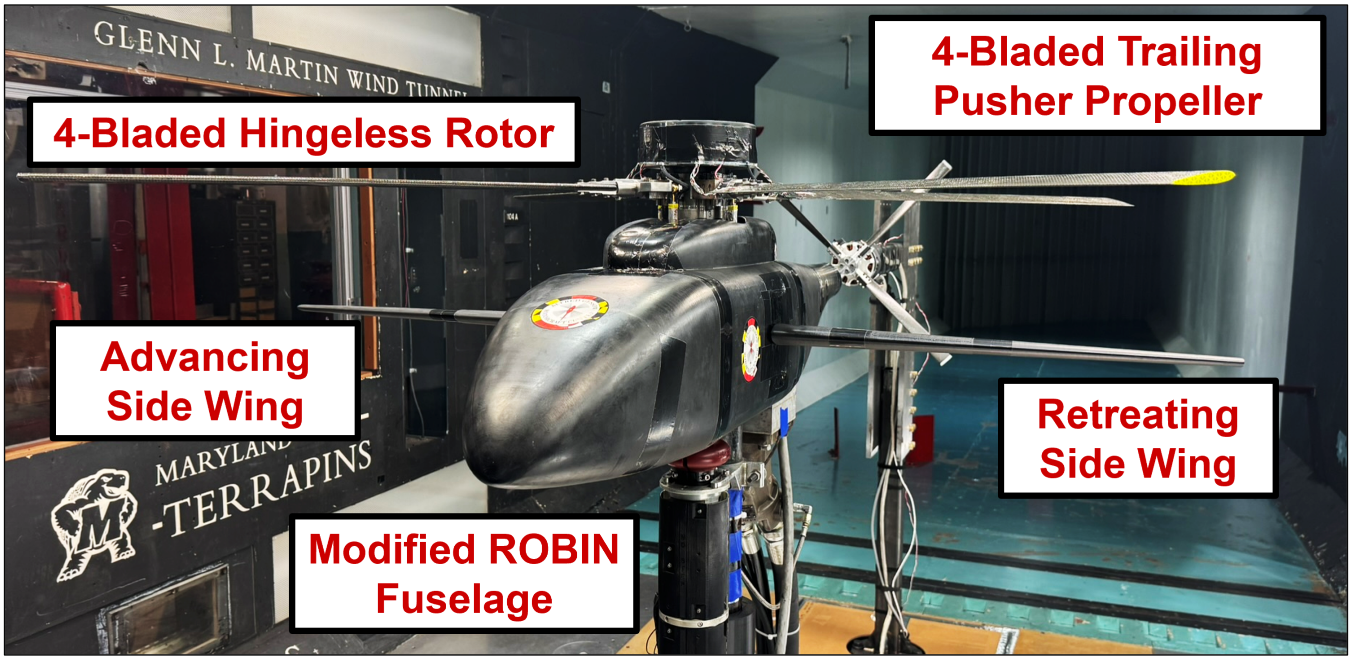

Figure 8. Test setup for lift and thrust-compounding in the Glenn L. Martin Wind Tunnel. The UMD Compound Rotorcraft Rig includes a full-span wing with separate balances for both the rotor and wing. The aft-mounted pusher propeller is installed on a dedicated stand with its own balance.

pound helicopter configurations across varying advance ratios, wing incidence angles, rotor shaft tilt angles, and lift trim targets. This study focuses on a subset of cases using 8° wing incidence and 0° rotor shaft tilt, based on prior findings that higher wing incidence improves aerodynamic performance, minimizes blade structural loads, and reduces vibratory loads (Refs. 5, 33). This restriction enables a consistent comparison of the six representative compound configurations. Table 2 summarizes the configurations included in the study.

Table 2. Test Matrix

Run no.	μ	Net C_L/σ	α_s	θ_w	Wing(s)
Lift Compound:					
U1	0.3, 0.5	0.03–0.06	0°	8°	None
U2	0.3, 0.5, 0.7	0.03–0.12	0°	8°	Half
U3	0.3, 0.5, 0.7	0.03–0.14	0°	8°	Full
Lift and Thrust Compound:					
U4	0.3, 0.4, 0.5	0.03–0.06	0°	8°	None
U5	0.3, 0.4, 0.5	0.03–0.12	0°	8°	Half
U6	0.3, 0.4, 0.5	0.03–0.13	0°	8°	Full

LIFT COMPOUNDING

The lift-compound configuration uses a fixed wing to offload the main rotor at high advance ratios. A pusher propeller is not present. The half-wing and full-wing lift compound configurations are compared to the isolated rotor configuration, which serves as the baseline. The aircraft performance, rotor control angles, blade structural loads, and hub vibratory loads for the various rotorcraft configurations are compared at $\theta_w = 8°$ and $\alpha_s = 0°$. Although the model was trimmed for wind tunnel equilibrium rather than propulsive trim, the resulting rotor blade drag and wing drag still represent a thrust requirement in forward flight. Assuming an ideal propeller with 100% efficiency, this drag is accounted for in C_X/σ and in the lift-to-drag ratio (L/D), allowing for consistent comparison across configurations.

This section first compares lift-compounded rotorcraft performance, rotor control angles, blade structural loads, and hub vibratory loads at an advance ratio of $\mu = 0.5$. A subsequent comparison examines performance and rotor control characteristics over a range of advance ratios.

Performance

Lift compounding has a strong influence on aircraft performance. Figure 9a shows the expected increase in wing lift share with increasing wing area. The half-wing and full-wing lift compound configurations are able to attain higher lift targets prior to rotor blade stall due to the wing lift share. At low lift targets, the full-wing configuration generates excess lift, requiring negative rotor thrust and resulting in a wing lift share exceeding 100%.

Wing lift share offloads the rotor, thereby reducing the required main rotor torque. Figure 9b illustrates a significant decrease in rotor torque for the lift compound configurations. The isolated rotor experiences a sharp increase in torque due to stall onset near $C_L/\sigma = 0.05$, while the lift-compound configurations remain in the low rotor lift regime at the same condition. Despite the large difference in wing lift share, the half-wing and full-wing configurations exhibit similar rotor torque. This is due to the lift offset present in the half-wing configuration, where the asymmetric wing lift distribution shifts the

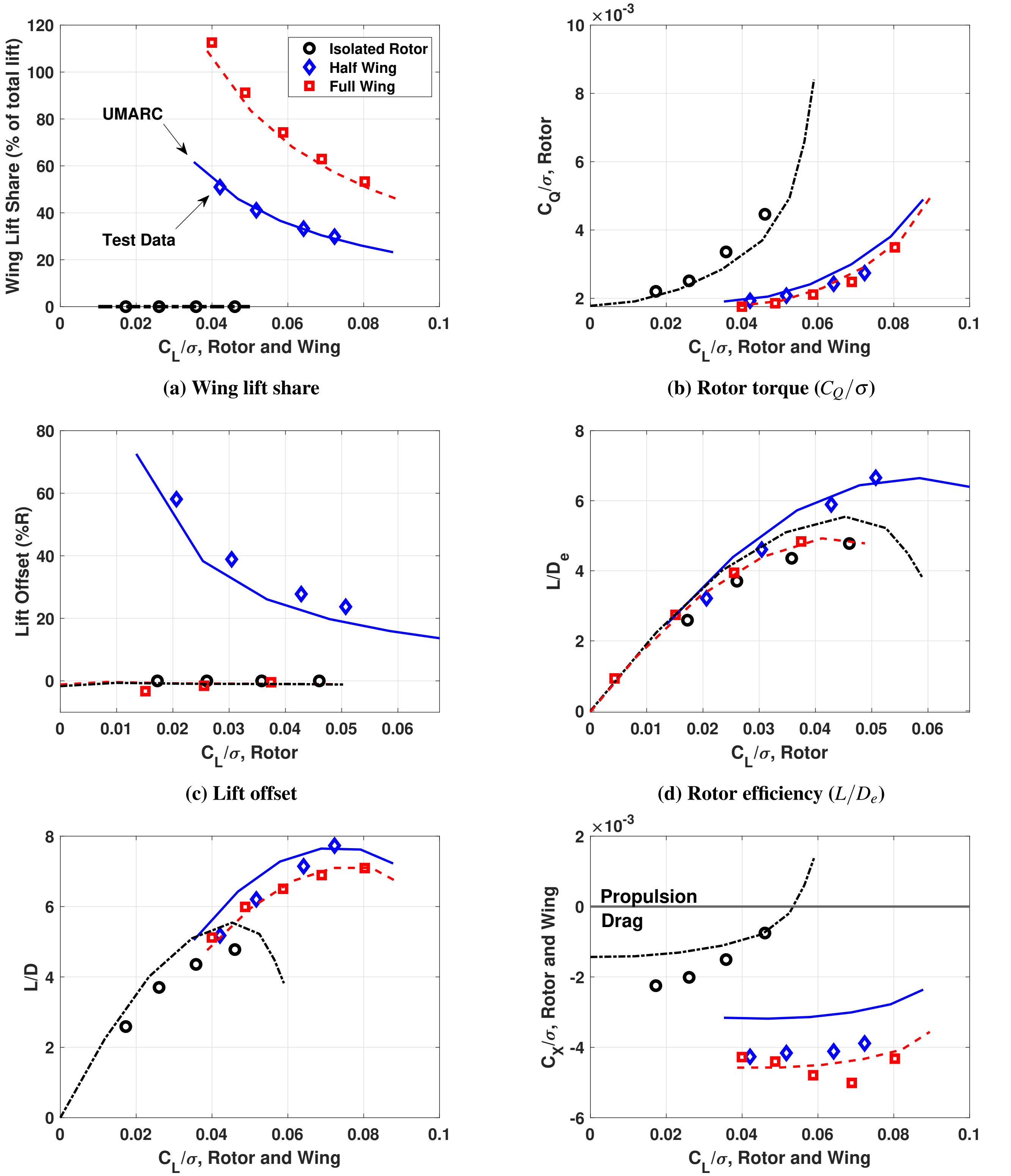

(a) Wing lift share

(b) Rotor torque (C_Q/σ)

(c) Lift offset

(d) Rotor efficiency (L/D_e)

(e) Rotor and wing combined lift-to-drag ratio (L/D)

(f) Rotor and wing X-force (C_X/σ)

Figure 9. Performance comparison of lift-compounded configurations at $\mu = 0.5$, $\alpha_s = 0°$, $\theta_w = 8°$. Symbols: Test Data, Lines: UMARC.

rotor's net lift vector outboard of $0.2R$ across all tested lift targets, as shown in Figure 9c. Lift offset magnitude increases as C_L/σ decreases since rotor loading is reduced while wing lift and the resulting rolling moment remain unchanged.

Combined rotor-wing and rotor-only performance are characterized by total lift-to-drag ratio (L/D) and rotor efficiency (L/D_e), respectively. L/D is defined in Equation 3. The rotor efficiency, L/D_e, is obtained by removing the wing contributions C_{L_W} and C_{D_W} from Equation 3.

$$
\begin{aligned}
L/D &= \frac{L_R + L_W}{D_e + D_W} \\
&= \frac{C_T \cos\alpha_s + C_H \sin\alpha_s + C_{L_W}}{C_Q/\mu + C_T \sin\alpha_s - C_H \cos\alpha_s + C_{D_W}}
\end{aligned}
\tag{3}
$$

Figure 9d shows that the full-wing and isolated rotor configurations achieve comparable rotor efficiency (L/D_e) due to similar trim states. In contrast, the lift offset inherent to the half-wing configuration enhances aerodynamic efficiency by shifting rotor lift toward the advancing side, where dynamic pressure is higher. This results in a 37% increase in peak L/D_e relative to the other configurations. The UMARC analysis indicates that the L/D_e peak shifts toward higher rotor lift when lift offset is present, as the asymmetric wing lift mitigates rotor dissymmetry. This reduces rotor cyclic pitch demand and delays the onset of blade stall to higher rotor lift values.

The half-wing configuration achieves the highest peak combined rotor and wing L/D, with a 62% increase over the isolated rotor configuration as shown in Figure 9e. Although the half wing contributes less wing lift than the full wing, the half-wing configuration still attains a 9% higher peak L/D due to lower wing drag. The full-wing configuration's additional advancing-side wing area increases total drag without the lift offset benefit, reducing its lift-to-drag ratio. Figure 9f shows combined rotor and wing drag ($-C_X/\sigma$) against rotor and wing lift. As expected, the isolated rotor exhibits the lowest total drag due to the absence of a wing. The half-wing configuration experiences lower drag than the full-wing configuration, consistent with its smaller planform area and higher L/D.

UMARC analysis satisfactorily captures rotor and wing performance trends and magnitudes. The analysis generally underpredicts C_X/σ and therefore slightly overpredicts L/D.

Rotor Control Angles

The collective (θ_{75}) required to trim the rotor to desired lift trim targets is shown in Figure 10. As expected, increasing wing area decreases the required collective angle for a given lift target. Hence, the collective trends resemble the corresponding rotor torque trends shown in Figure 9b. Lift offset enables the half-wing configuration to generate greater rotor lift for a given collective pitch setting compared to the full-wing configuration.

Cyclic blade pitch control angles used to maintain wind tunnel trim are shown in Figure 11. As wing lift share increases,

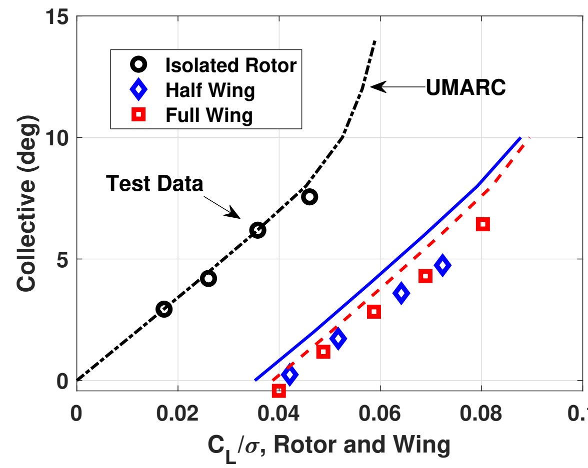

Figure 10. Rotor collective vs rotor and wing combined lift for various configurations. $\mu = 0.5$, $\alpha_s = 0°$, $\theta_w = 8°$. Symbols: Test Data, Lines: UMARC.

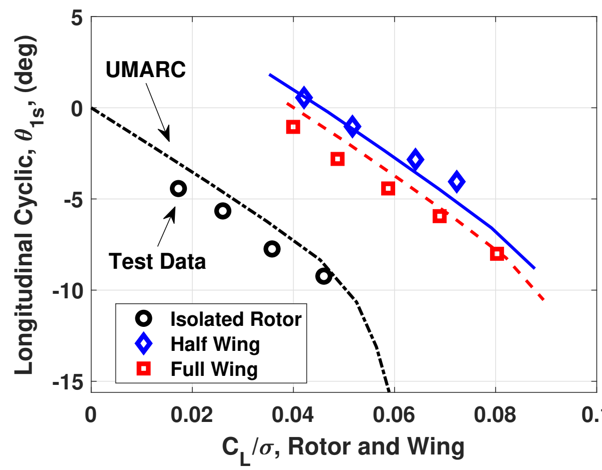

(a) Longitudinal Cyclic (θ_{1s})

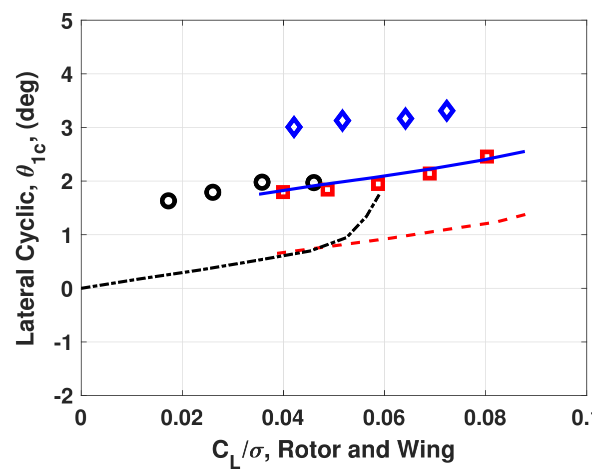

(b) Lateral Cyclic (θ_{1c})

Figure 11. Main rotor cyclic control angles for various configurations. $\mu = 0.5$, $\alpha_s = 0°$, $\theta_w = 8°$. Symbols: Test Data, Lines: UMARC.

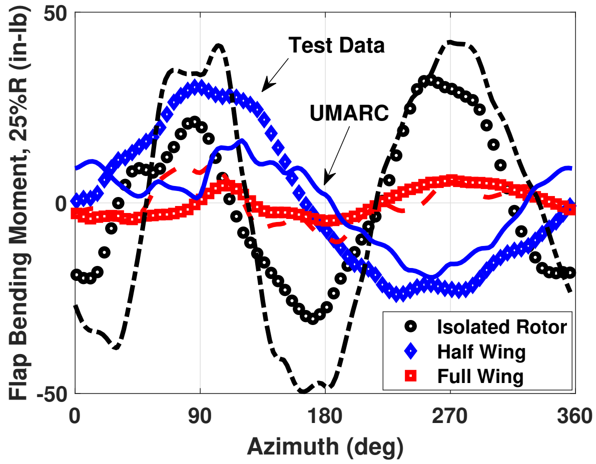

(a) Flap Bending Moment Variation

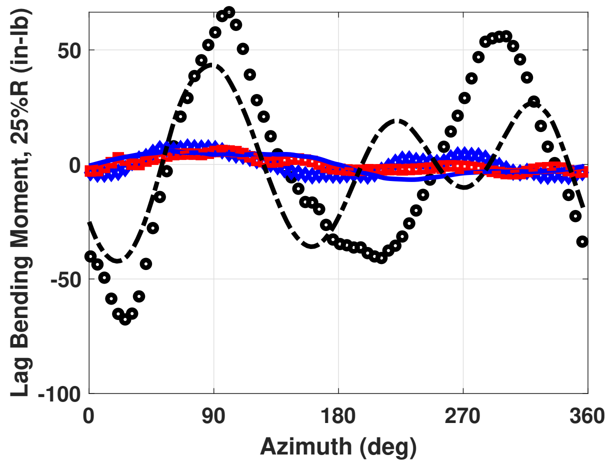

(b) Lag Bending Moment Variation

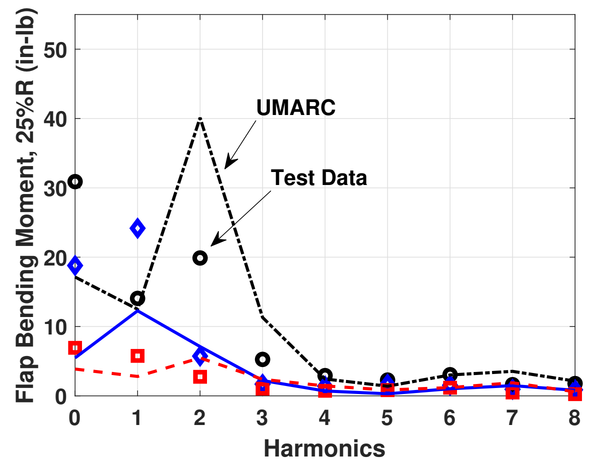

(c) Flap Bending Moment Harmonics

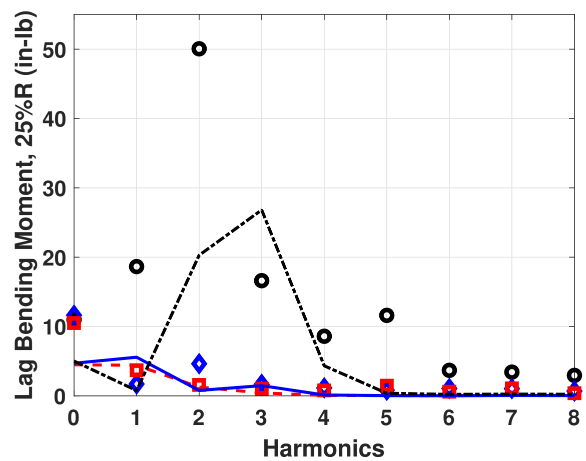

(d) Lag Bending Moment Harmonics

Figure 12. Blade structural loads at 25%R. $C_L/\sigma = 0.048$, $\mu = 0.5$, $\alpha_s = 0°$, $\theta_w = 8°$. **Symbols: Test Data, Lines: UMARC.**

longitudinal cyclic input decreases due to the reduction in rotor lift contribution. This is accompanied by a decrease in collective pitch, which lessens the need to compensate for lift dissymmetry across the rotor disk. Additionally, the introduction of lift offset further reduces longitudinal cyclic demand by leveraging the rolling moment generated by the asymmetric wing to counteract rotor airflow asymmetry. Lateral cyclic remains largely unchanged with symmetric wing lift sharing. The isolated rotor and full-wing lift-compounded configurations share similar trim states. In contrast, the half-wing configuration exhibits increased lateral cyclic demand relative to the isolated rotor, attributed to increased 1/rev blade flapping induced by lift offset. Additionally, abrupt changes in cyclic pitch magnitudes are observed in the isolated rotor case near $C_L/\sigma = 0.05$, corresponding to the onset of blade stall.

UMARC accurately predicts collective and longitudinal cyclic control angles and captures the overall trend in the lateral cyclic control angle, although it underpredicts its magnitude. This discrepancy arises from unmodeled aerodynamic moments on the rotor hub, which generate a significant positive pitching moment (M_Y) in the test. To maintain trim, this moment is countered by increased positive lateral cyclic, a response not captured in UMARC due to the absence of hub aerodynamic modeling.

Blade Structural Loads

Figures 12a and 12b present blade flap and lag bending moments over one rotor revolution at $\mu = 0.5$ and $C_L/\sigma = 0.048$, with steady loads removed. Half peak-to-peak harmonic amplitudes, extracted by harmonic decomposition, are shown in Figures 12c and 12d.

The isolated rotor and full-wing configurations are both trimmed to zero hub moments, resulting in relatively symmetric flap bending moments on the advancing and retreating sides of the rotor disk. Peak flap bending moments occur near 90° and 270° azimuths, indicating a dominant 2/rev harmonic in these symmetric cases. The 2/rev flap bending moment decreases by 86% from the isolated rotor to the full-wing configuration due to lift sharing between the rotor and

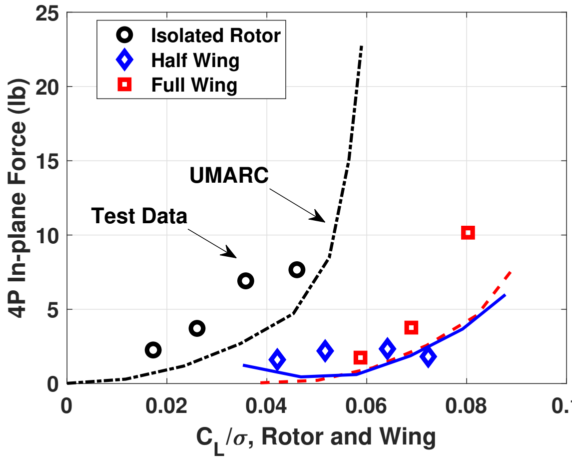

(a) **4P In-plane Hub Vibratory Load (F_{XY})**

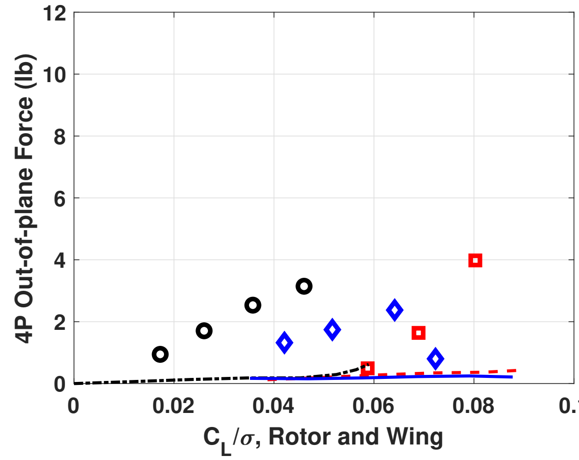

(b) **4P Out-of-plane Hub Vibratory Load (F_Z)**

Figure 13. 4P Hub vibratory loads. $\mu = 0.5$, $\alpha_s = 0°$, $\theta_w = 8°$. Symbols: Test Data, Lines: UMARC.

wing. The half-wing configuration exhibits a dominant 1/rev flap bending moment driven by lift offset. The retreating side flap bending moment is negative, unlike the other configurations, since lift demand in this region is reduced. The retreating side flap bending moment becomes negative, reflecting reduced lift demand in that region. Compared to the isolated rotor, the half-wing configuration exhibits a 73% increase in the 1/rev harmonic and a 71% reduction in the 2/rev component. Rotor-wing lift sharing directly affects the steady flap bending moment. The half-wing configuration reduces the steady flap moment by 39% relative to the isolated rotor, while the full-wing configuration achieves a larger reduction of 78%. UMARC predictions effectively capture the trends in harmonic modes. The azimuthal variation of the flap bending moment is fairly well predicted.

The lag bending moment exhibits significant components at both the 2/rev and 3/rev harmonics. Compared to the isolated rotor, lift compounding reduces these 2/rev and 3/rev lag bending moments by approximately 90% in both the half-wing and full-wing configurations. UMARC predictions are satisfactory for the configurations with low rotor loading. Discrepancies arise at higher rotor loads, primarily due to uncertainties in the measured blade chordwise stiffness (EI_c).

The full-wing configuration offers the greatest reduction in peak-to-peak blade structural loads, decreasing flap and lag bending moments by 61% and 88%, respectively, compared to the isolated rotor configuration.

The rotor blades were instrumented with strain gages to measure the torsional moment; however, the high-frequency torsional response limited the resolution of the data. Therefore, the torsion moment measurements are not shown.

Hub Vibratory Loads

Figure 13 shows 4P hub vibratory forces in the in-plane and out-of-plane directions. The in-plane vibratory forces are defined as the norm of the loads in the X (longitudinal) and Y (lateral) directions, defined in Equation 4.

$$F_{xy} = \sqrt{F_X^2 + F_Y^2} \tag{4}$$

In-plane vibratory loads increase with rotor loading. A significant increase is observed with the onset of blade stall. Vibratory loading is similar for the half-wing and full-wing conditions, owing to decreased rotor collective and cyclic blade pitch control angles. UMARC accurately predicts the trends in in-plane vibratory loads. The 4P out-of-plane vibratory loads exhibit a modest increase with rotor loading, but their magnitudes remain less than half of the corresponding in-plane vibration levels. These vertical vibratory loads scale primarily with rotor lift, showing limited sensitivity to lift offset effects. Hence, the full-wing configuration experiences the lowest out-of-plane vibration as it features the greatest wing lift share. UMARC does not predict the increase in vertical vibratory loading with rotor loading.

Figure 14 shows 4P hub vibratory moments in the rolling and pitching directions. The trends closely mirror those observed in the in-plane vibratory forces: increasing wing lift share and lift offset reduce vibratory moments. The half-wing configuration generates comparable X-axis (rolling) vibratory moments to the full-wing configuration, but is less effective in reducing Y-axis (pitching) vibrations.

Overall, lift compounding effectively reduces vibratory loads by both unloading the rotor and introducing a beneficial lift offset.

Influence of Advance Ratio on Performance and Rotor Control Angles

The effect of varying advance ratio on vehicle performance and rotor control angles was examined for the half-wing and

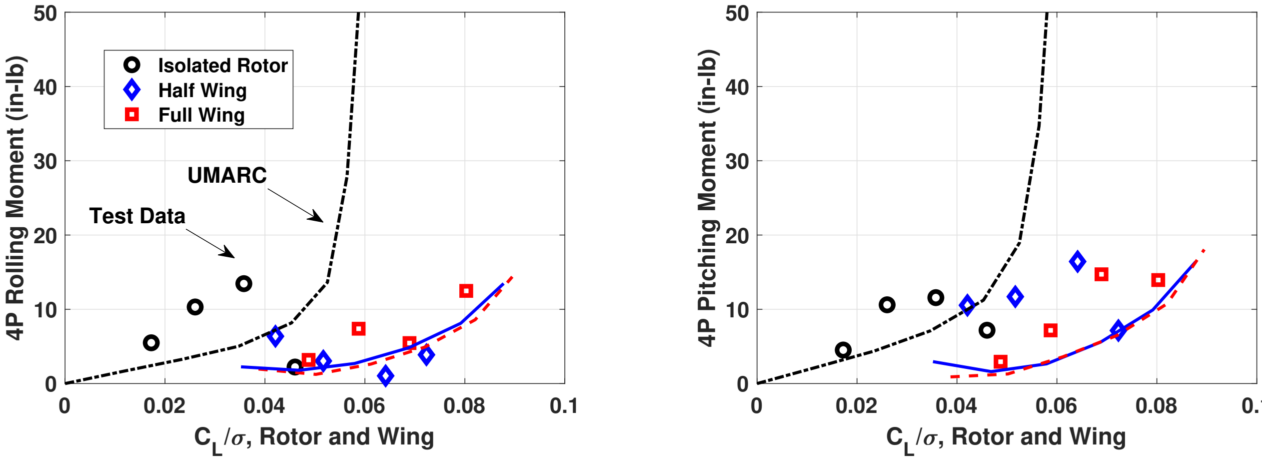

(a) 4P Hub Rolling Moment (M_X) **(b) 4P Hub Pitching Moment (M_Y)**

Figure 14. 4P Hub vibratory moments. $\mu = 0.5$, $\alpha_s = 0°$, $\theta_w = 8°$. **Symbols: Test Data, Lines: UMARC.**

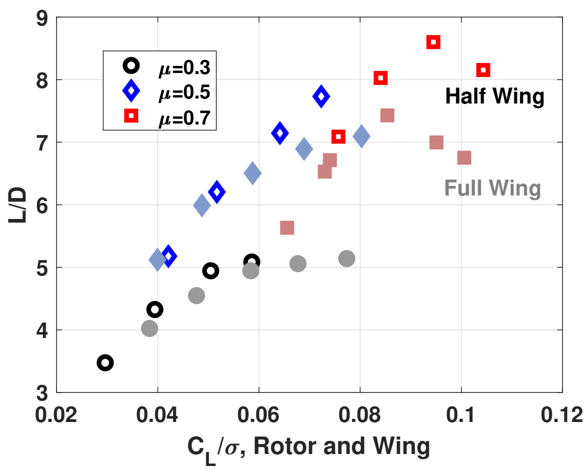

Figure 15. Rotor and wing combined lift to drag ratio. $\alpha_s = 0°$, $\theta_w = 8°$. **Hollow points: half wing, Filled points: full wing.**

full-wing lift compound configurations. The cases shown span $\mu = 0.3 - 0.7$.

Figure 15 shows the rotor and wing combined lift-to-drag ratio. L/D increases with advance ratio as wing lift increases. An increase in advance ratio corresponds to an increase in forward flight speed, as the rotor speed remains constant. The rotor generates the majority of total lift at low advance ratios since the wings are ineffective at slow speeds; hence, the half-wing and full-wing L/D values are similar. The half-wing configuration attains a maximum L/D of 8.6, 14% greater than the full-wing configuration at $\mu = 0.7$. To investigate this trend, Figure 16 shows wing lift share, wing drag contribution, and rotor performance metrics. As illustrated in Figure 16a, the full-wing configuration consistently offloads approximately twice as much rotor lift to the wing as the half-wing configuration across all advance ratios. However, Figure 16b indicates that the advancing side wing introduces significantly more wing drag, leading to a net increase in total drag and a corresponding reduction in L/D compared to the half-wing configuration. Prior to its L/D peak, the full-wing configuration offloads more than 100% of the desired lift from the rotor, resulting in negative rotor thrust while rotor torque remains largely unchanged, as shown in Figure 16c. This condition reduces rotor efficiency, seen in Figure 16d. In contrast, the half-wing configuration leverages increased lift offset to maintain higher rotor efficiency at high advance ratios, shown in Table 3.

Table 3. Lift Offset at Rotor $C_L/\sigma = 0.05$

μ	Lift Offset (%R)	C_L/σ Rotor and Wing
0.3	8.3	0.059
0.5	24.2	0.072
0.7	43.5	0.089

Figure 17 shows the variation of cyclic control angles with advance ratio. As the advance ratio increases, the longitudinal cyclic demand rises more steeply due to the expansion of the retreating side reverse flow region, necessitating greater compensation for lift dissymmetry. In the half-wing configuration, lift offset increases with advance ratio, producing a counteracting rolling moment that mitigates rotor lift asymmetry and reduces the required longitudinal cyclic input. Countering the rotor's forward flight dissymmetry with the wing's rolling moment, rather than longitudinal cyclic, may delay thrust reversal to higher advance ratios. The lateral cyclic control angle remains relatively constant for the full-wing configuration at all advance ratios since there is no rotor shaft tilt. In contrast, the half-wing configuration requires an increase in lateral cyclic input at higher advance ratios, driven by greater 1/rev blade flapping associated with the greater lift offset magnitude (Ref. 33).

Aerodynamic Interaction

The UMARC MFW model captures the trajectories and distortion of rotor and wing trailed vortices. Figure 18 illustrates the free-wake geometry for the half-wing and full-wing

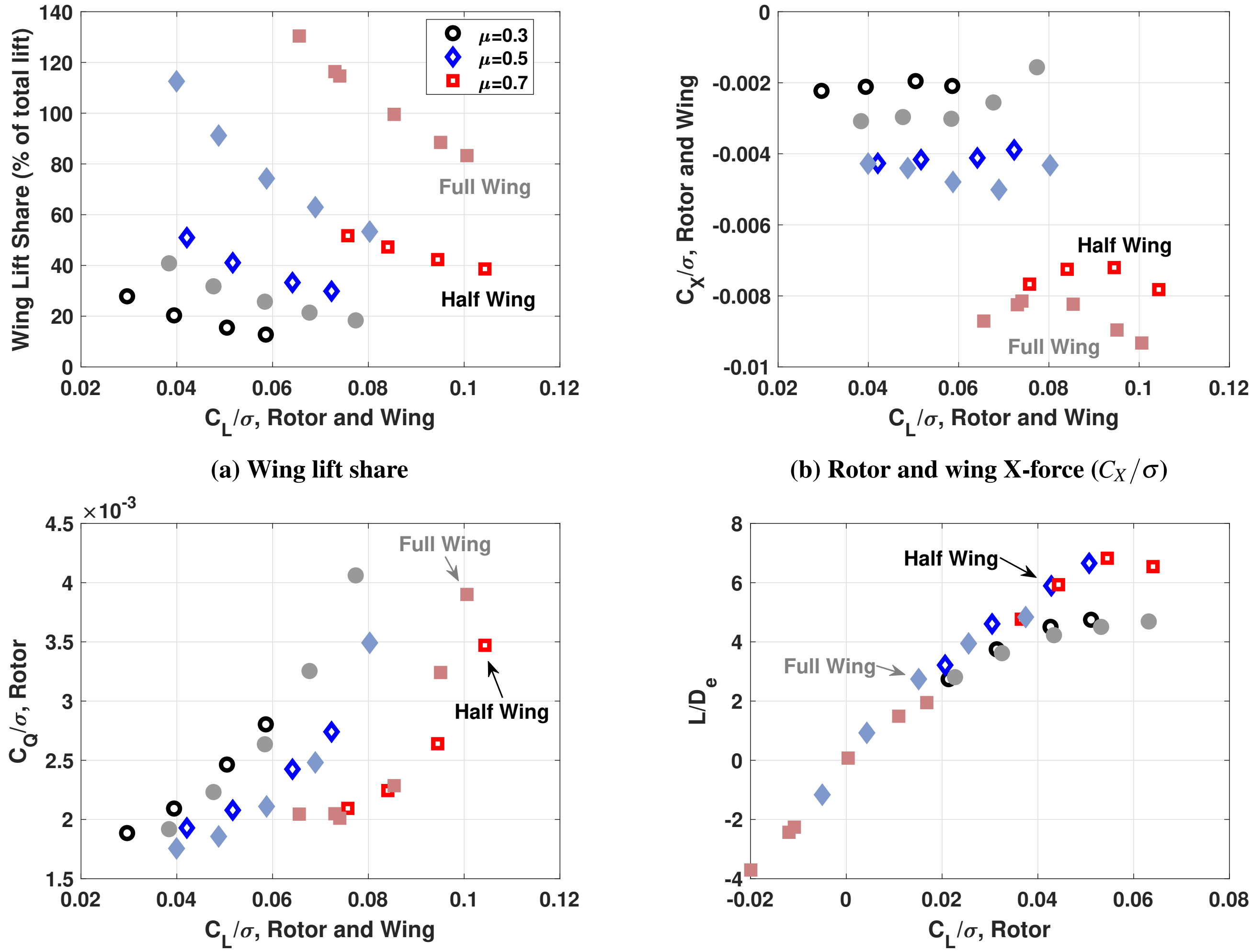

(a) Wing lift share

(b) Rotor and wing X-force (C_X/σ)

(c) Rotor torque (C_Q/σ)

(d) Rotor efficiency (L/D_e)

Figure 16. Performance metrics of lift-compounded configurations at varying advance ratios. $\alpha_s = 0°$, $\theta_w = 8°$. Hollow points: half wing, Filled points: full wing.

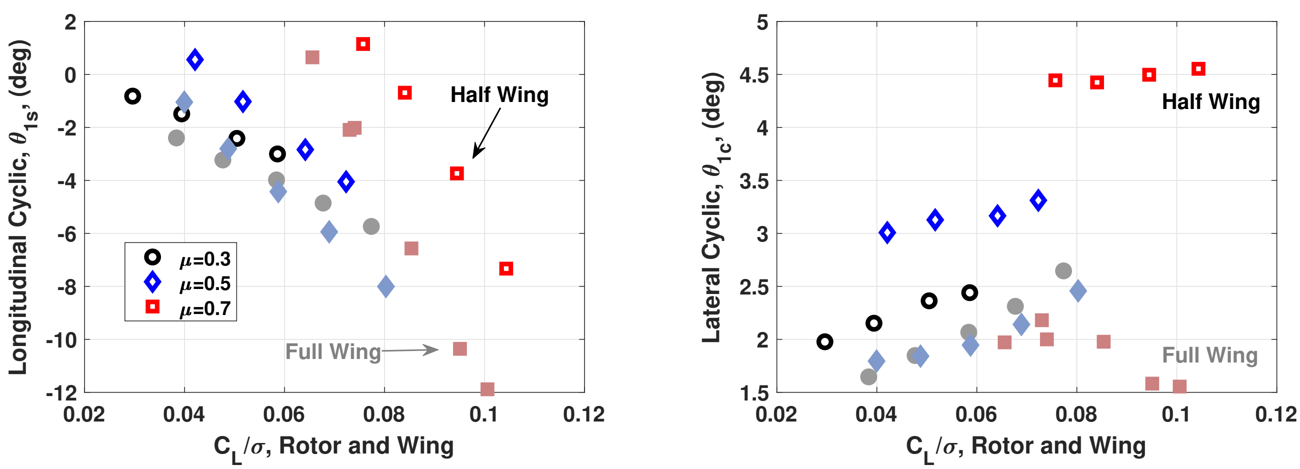

(a) Longitudinal Cyclic (θ_{1s})

(b) Lateral Cyclic (θ_{1c})

Figure 17. Cyclic control angles at varying μ. $\alpha_s = 0°$, $\theta_w = 8°$. Hollow points: half wing, Filled points: full wing.

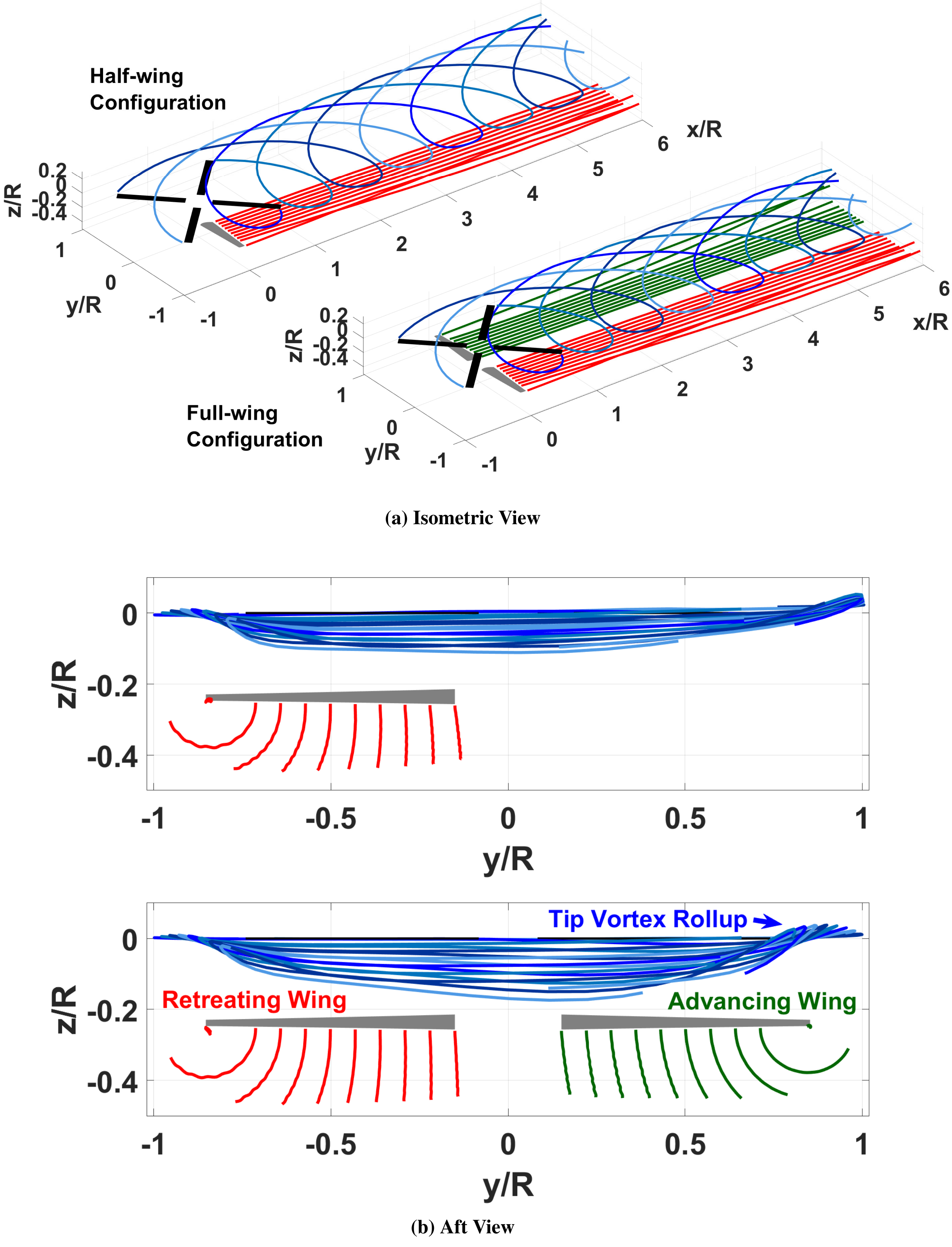

Figure 18. Free wake geometry for the lift-compounded configurations at net $C_L/\sigma = 0.048$ and $\mu = 0.5$. $\alpha_s = 0°$, $\theta_w = 8°$.

lift-compounded configurations at a net $C_L/\sigma = 0.048$. At $\mu = 0.5$, the rotor wake is convected downstream rapidly, avoiding direct wing impingement. Although the full-wing configuration generates lower rotor thrust than the half-wing configuration, the increased wing downwash strength distorts the rotor wake downwards more than the half-wing configuration. This effect may be relevant for configurations employing large-diameter trailing pusher propellers, where increased downwash could lead to partial ingestion of the rotor wake by the propeller.

LIFT AND THRUST COMPOUNDING

The lift and thrust-compounded configuration builds upon the lift-compounded setup by incorporating a trailing pusher propeller to augment propulsive thrust. The main rotor and wing exhibit performance trends similar to those of the lift-compounded configuration. Accurately characterizing the propeller and understanding its impact on overall vehicle performance is essential for translating wind tunnel data to free-flight applications of lift and thrust-compounded rotorcraft.

Propeller Characterization

The aerodynamic performance of the propeller is highly sensitive to the inflow, which arises from the combination of tunnel freestream velocity, flow blockage from the wings and fuselage, and propeller rotational speed. Cruise inflow (λ_c) is defined in Equation (5).

$$\lambda_c = \frac{V}{\Omega_p R_p} \tag{5}$$

Figure 19a shows the effect of wing configuration on propeller thrust. Thrust decreases with increasing λ_c. The half-wing lift and thrust-compound configuration marginally decreases propeller thrust at a set cruise inflow compared to the symmetric configurations. Figure 19b shows that propeller torque increases steadily with thrust, as expected. The wing wake has a minimal effect on propeller torque. Propulsive efficiency, shown in Figure 19c, is defined in Equation (6).

$$\eta_p = \frac{P_{ideal}}{P_{actual}} = \frac{C_T \lambda_c}{C_P} \tag{6}$$

Propulsive efficiency is determined using an idealized cruise inflow, assuming uniform and undisturbed free-stream conditions. However, flow blockage from the fuselage reduces the effective velocity reaching the propeller, leading to an overrepresentation of the actual propulsive efficiency. The marginal reduction in propeller thrust at all cruise inflows for the half-wing configuration compared to the symmetric configurations manifests as a reduction in propulsive efficiency, especially at higher λ_c. In contrast, although the full-span wings in the full-wing configuration are located upstream of the propeller and produce a downstream wake, they do not significantly impact propulsive efficiency relative to the thrust-compound configuration without wings.

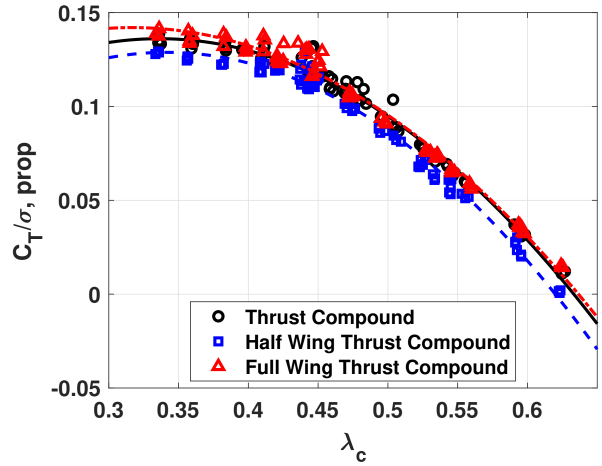

(a) Propeller Thrust

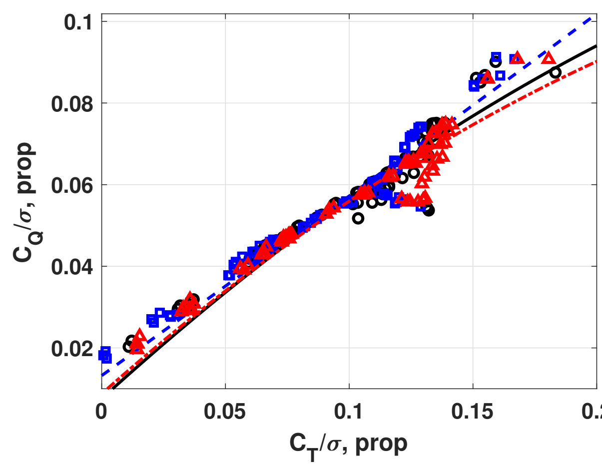

(b) Propeller Torque

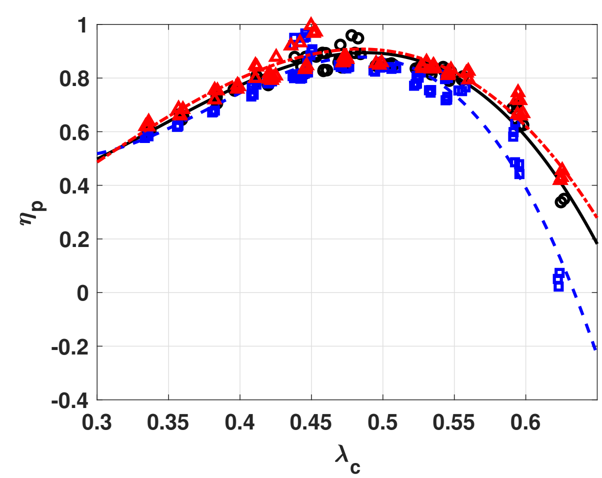

(c) Propulsive Efficiency

Figure 19. Propeller performance characterization. Symbols: Test Data. Lines: Trendlines.

Total Vehicle Performance

The lift and thrust-compounded test model achieved propulsive trim up to $\mu = 0.5$. Propulsive trim is reached when the propeller produces thrust that balances the total aerodynamic drag from the fuselage, rotor, wings, and the propeller itself. Full-vehicle lift to drag ratio, defined in Equation 7, can be obtained to approximate the performance of an equivalent free-flying aircraft.

$$L/D = \frac{TV_\infty}{P} = \frac{C_L \mu}{C_{Q,\text{rotor}} + C_{Q,\text{prop}}} \tag{7}$$

Fuselage drag was not actively measured during rotor operation. Instead, it was measured independently prior to the test campaign. Details on the fuselage drag measurement and methodology are documented in Reference 5.

Figure 20 shows the full-vehicle lift-to-drag ratio for the thrust-compound configuration, the half-wing lift and thrust-compound configuration, and the full-wing lift and thrust-compound configuration. The results are shown up to an advance ratio of $\mu = 0.5$, beyond which the propeller reached the maximum rated power limit. The total vehicle lift-to-drag ratio increases with net lift across all configurations. Peak L/D decreases with advance ratio for the thrust-compounded configuration, consistent with the expected decline in performance for an isolated rotor at high advance ratios. The half-wing and full-wing lift and thrust-compounded configurations both achieve greater wing lift sharing as advance ratio increases, leading to improved lift-to-drag ratio with forward speed. At $\mu = 0.5$, the two configurations yield nearly identical L/D values for this specific rotorcraft model. The maximum measured lift-to-drag ratio reaches 4.5 at $\mu = 0.5$, representing an 18% improvement over the L/D at $\mu = 0.3$.

Figure 21 presents the ratio of propeller power to rotor power ($P_{\text{prop}}/P_{\text{rotor}}$) across various advance ratios. As the lift target increases, rotor thrust and torque increase, resulting in a corresponding decrease in the power ratio. At $\mu = 0.3$, the propeller consumes less power than the main rotor across all configurations. However, at $\mu = 0.5$, all configurations require greater propeller power due to elevated fuselage and wing drag. Among them, the full-wing lift and thrust-compounded configuration produces the highest drag and demands 2.8 times more propeller power than rotor power to maintain propulsive trim at $\mu = 0.5$.

CONCLUSIONS

A wind tunnel investigation was conducted in the Glenn L. Martin Wind Tunnel to investigate the performance characteristics of a compound helicopter equipped with various lift and thrust compounding elements operating at high advance ratios. Experimental measurements of performance, blade loads, and hub vibratory loads were acquired up to $\mu = 0.7$ to validate the UMARC comprehensive analysis model. The results focused on evaluating the relative effectiveness of half-wing and full-wing lift compounding strategies, both with and

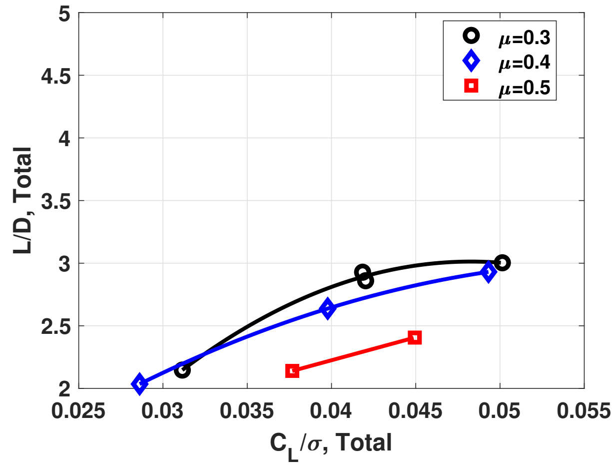

(a) Thrust-compounded configuration

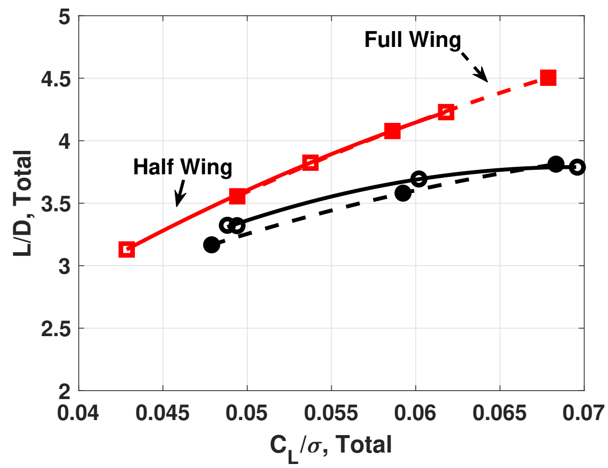

(b) Lift and thrust-compounded configurations

Figure 20. Lift-to-drag ratio (L/D) of the propulsive-trimmed compound configurations. $\alpha_s = 0°$, $\theta_w = 8°$. Symbols: Test data. Lines: Trendlines.

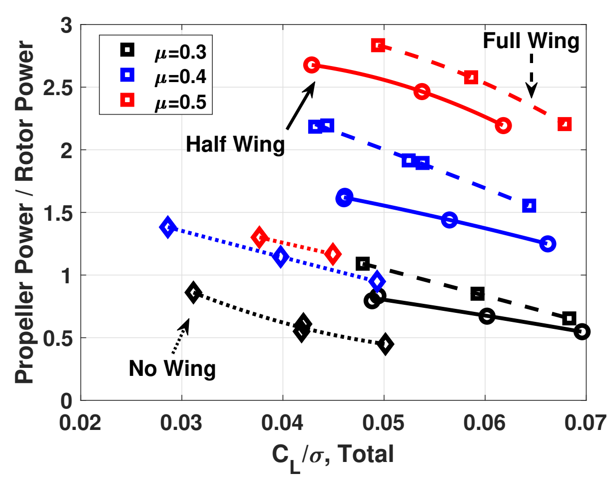

Figure 21. Propeller-rotor power ratio at varying μ. $\alpha_s = 0°$, $\theta_w = 8°$. Symbols: Test data. Lines: Trendlines.

without pusher propeller thrust augmentation. The primary objective of this investigation was to gain insight into the attributes of efficient high-speed compound helicopters with the aim of informing future design decisions. The following conclusions are drawn from this research:

1. Half-wing lift compounding attains the best high speed performance with a maximum $L/D = 8.6$ at $\mu = 0.7$ using lift offset. The full-wing lift compound configuration suffers from reduced rotor efficiency and increased wing drag, achieving a peak L/D of only 7.4 under the same flight condition.

2. Wings are detrimental in hover due to downwash from rotor wake impingement. The full-wing configuration exhibits a 4.5% reduced figure of merit at high collective angles.

3. Significant wing-rotor wake interaction is present at $\mu = 0.5$ as strong wing downwash deflects the rotor wake downwards. This interaction may result in undesirable partial rotor wake ingestion for compound configurations employing large-diameter trailing pusher propellers.

4. Full-wing lift compounding most effectively reduces peak-to-peak blade structural loads of all the tested configurations. At $\mu = 0.5$ and net $C_L/\sigma = 0.048$, flap and lag bending moments decrease by 61% and 88%, respectively, compared to the isolated rotor.

5. The steady flap bending moment is greatly reduced with increased wing lift sharing. The steady flap moment decreases by 39% and 78% for the half-wing and full-wing configurations, respectively, compared to the isolated rotor at $\mu = 0.5$.

6. Lift compounding significantly reduces hub vibratory loads compared to the isolated rotor. The half-wing and full-wing configurations exhibit similar reduction in vibratory loads despite differing aerodynamic contributions: the half-wing introduces lift offset while the full-wing shares a greater portion of the total lift.

7. UMARC comprehensive analysis satisfactorily captures compound rotorcraft performance in hover and forward flight. Blade structural loads predictions generally followed correct trends, but can be improved with more accurate measurements of blade structural properties.

8. Achieving propulsive trim at high advance ratios necessitates substantial propeller power compared to main rotor power. At $\mu = 0.5$, the full-wing lift and thrust-compounded configuration demanded 2.8 times more propeller power than rotor power to maintain trim.

Author contact:

Vivek Uppoor vvuppoor@gmail.com
Inderjit Chopra chopra@umd.edu

FUTURE WORK

This study concludes the fundamental aeromechanics investigation of lift and thrust compound helicopter configurations. Future work will involve measuring the aerodynamic interactions between the rotor, wing, and propeller using Particle Image Velocimetry (PIV) and smoke flow visualization to capture the intricate coupling necessary for accurate analytical modeling. The fuselage flow blockage into the propeller will also be quantified.

ACKNOWLEDGEMENTS

This work was conducted at the Alfred Gessow Rotorcraft Center under the Army/Navy/NASA Vertical Lift Research Center of Excellence (VLRCOE) program, with technical monitor Dr. Mahendra Bhagwat. The authors thank Howard Zheng and Radu Teodorescu for their assistance in preparing and conducting the wind tunnel tests.

REFERENCES

1. Floros, M. W., and Johnson, W., "Performance Analysis of the Slowed-Rotor Compound Helicopter Configuration," *Journal of the American Helicopter Society*, Vol. 54, (2), April 2009, pp. 1–12. DOI: 10.4050/JAHS.54.022002.

2. Datta, A., Yeo, H., and Norman, T. R., "Experimental Investigation and Fundamental Understanding of a Full-Scale Slowed Rotor at High Advance Ratios," *Journal of the American Helicopter Society*, Vol. 58, (2), April 2013, pp. 1–17. DOI: 10.4050/JAHS.58.022004.

3. Johnson, W., "Influence of Lift Offset on Rotorcraft Performance," NASA TP 2009-215404, November 2009.

4. Kaplan, N., Patil, M., Chopra, I., and Datta, A., "Wind Tunnel Testing and Aeromechanics Predictions on Slowed Mach-scaled Thrust Compounding Rotorcraft with a Trailing Propeller," Proceedings of the Vertical Flight Society International 79th Annual Forum & Technology Display, West Palm Beach, FL, May 16–18, 2023.

5. Uppoor, V., Zheng, H., and Chopra, I., "High Advance Ratio Wind Tunnel Testing of a Slowed Mach-scaled Rotor with Full-Wing and Trailing Propeller Lift and Thrust Compounding," Proceedings of the Vertical Flight Society International 81st Annual Forum & Technology Display, May 20-22, 2025.

6. Hislop, G. S., "The Fairey Rotodyne," *The Journal of the Helicopter Association of Great Britain*, Vol. 13, (1), February 1959, pp. 1–49.

7. Harris, F. D., "An Overview of Autogyros and The McDonnell XV-1 Convertiplane," NASA CR 2003-212799, October 2003.

8. Ruddell, A. J., "XH-59A ABC Technology Demonstratory Altitude Expansion and Operational Tests," USAAVRADCOM TR 81-D-35, December 1981.

9. Erickson, R. E., Cross, J. L., Kufield, R. M., Acree, C. W., Nguyen, D., and Hodge, R. W., "NASA rotor systems research aircraft: Fixed-wing configuration flight-test results," NASA Technical Memorandum 85363, September 1986.

10. Wyrick, D. R., "Extension of the High-Speed Flight Envelope of the XH-51A Compound Helicopter," USAAVLABS TR 65-71, November 1965.

11. Hohenemser, K. H., "Hingeless Rotor Flight Dynamics," Advisory Group for Aerospace Research and Development, North Atlantic Treaty Organization AGARD-AG-197, Sep. 1974.

12. Spreuer, W. E., "Experimental Flight Tests of the XH-51A Compound Helicopter," *Journal of the American Helicopter Society*, Vol. 13, (3), July 1969, pp. 64–69.

13. Johnson, W., Yamauchi, G. K., and Watts, M. E., "NASA Heavy Lift Rotorcraft Systems Investigation," NASA Technical Publication NASA/TP-2005-213467, December 2005.

14. Ormiston, R. A., "Revitalizing Advanced Rotorcraft Research - and the Compound Helicopter," *Journal of the American Helicopter Society*, Vol. 61, (1), January 2016, pp. 1–23. DOI: 10.4050/JAHS.61.011001.

15. Öhrle, C., Frey, F., Thiemeier, J., Keßler, M., Krämer, E., Embacher, M., Cranga, P., and Eglin, P., "Compound Helicopter X^3 in High-Speed Flight: Correlation of Simulation and Flight Test," Proceedings of the 75th Annual Forum of the Vertical Flight Society, Philadelphia, PA, May 13–16, 2019.

16. Eglin, P., Embacher, M., Desvigne, D., and Roca-Leon, E., "Airbus RACER High Speed Demonstrator Flight Tests," Proceedings of the Vertical Flight Society International 81st Annual Forum & Technology Display, May 20-22, 2025.

17. Blackwell, R., and Millott, T., "Dynamics Design Characteristics of the Sikorsky X2 Technology™ Demonstrator Aircraft," Proceedings of the 64th Annual Forum of the American Helicopter Society, Montreal, Canada, Apr-May 29–1, 2008.

18. Walsh, D., Weiner, S., Arifian, K., Lawrence, T., Wilson, M., Millott, T., and Blackwell, R., "High Airspeed Testing of the Sikorsky X2 Technology™ Demonstrator," Proceedings of the 67th Annual Forum of the American Helicopter Society, Virginia Beach, VA, May 3–5, 2011.

19. Nagaraj, V. T., and Chopra, I., "Dynamics Considerations for High Speed Flight of Compound Helicopters," Proceedings of the 58th Annual Forum of the American Helicopter Society, Montreal, Canada, June 11–13, 2002.

20. Yeo, H., and Johnson, W., "Optimum Design of a Compound Helicopter," *Journal of Aircraft*, Vol. 46, (4), July 2009, pp. 1210–1221. DOI: 10.2514/1.40101.

21. Moodie, A., and Yeo, H., "Design of a Cruise Efficient Compound Helicopter," *Journal of the American Helicopter Society*, Vol. 57, (3), July 2011, pp. 1–11. DOI: 10.4050/JAHS.57.032004.

22. Sridharan, A., Govindarajan, B., Nagaraj, V. T., and Chopra, I., "Design Considerations of a Lift-Offset Single Main Rotor Compound Helicopter," American Helicopter Society Technical Meeting on Aeromechanics Design for Vertical Lift, San Francisco, CA, January 20–22, 2016.

23. Escobar, D., and Yeo, H., "Performance and Loads of a Wing-Offset Compound Helicopter," *Journal of the American Helicopter Society*, Vol. 68, (3), July 2023, pp. 2–14. DOI: 10.4050/JAHS.68.032002.

24. Sugawara, H., Tanabe, Y., and Kameda, M., "Effect of Lift-Share Ratio on Aerodynamic Performance of Winged Compound Helicopter," *Journal of Aircraft*, Vol. 58, (5), September 2021, pp. 997–1009. DOI: 10.2514/1.C036163.

25. Frey, F., Thiemeier, J., Öhrle, C., Keßler, M., and Krämer, E., "Aerodynamic Interactions on Airbus Helicopters' Compound Helicopter RACER in Hover," *Journal of the American Helicopter Society*, Vol. 67, (1), January 2022, pp. 1–17. DOI: 10.4050/JAHS.67.012007.

26. Frey, F., Thiemeier, J., Öhrle, C., Keßler, M., and Krämer, E., "Aerodynamic Interactions on Airbus Helicopters' Compound Helicopter RACER in Cruise Flight," Proceedings of the Vertical Flight Society International 75th Annual Forum & Technology Display, May 13-16, 2019.

27. Brouwers, E., Fillman, M., and Deresz, R., "Advanced AH-64 Compound Wind Tunnel Testing Overview," Proceedings of the 75th Annual Forum of the American Helicopter Society, Philadelphia, PA, May 13–16, 2019.

28. Rivera, A. F., Lorber, P. F., Hein, B. R., Wallace, B., Dziuba, D., and Sargent, C., "Performance Wind Tunnel Testing of an X2 Technology Mach-Scaled Powered Model," Proceedings of the Vertical Flight Society International 81st Annual Forum & Technology Display, May 20-22, 2025.

29. Bowen-Davies, G., and Chopra, I., "Performance and Loads Predictions of a Mach-Scaled Rotor at High Advance Ratios," *Journal of the American Helicopter Society*, Vol. 61, (3), July 2016, pp. 1–11. DOI: 10.4050/JAHS.61.032008.

30. Wang, X., Bauknecht, A., Maurya, S., and Chopra, I., "Slowed Hingeless Rotor Wind Tunnel Tests and Validation at High Advance Ratios," *Journal of Aircraft*, Vol. 58, (1), January, pp. 153–166.

31. Maurya, S., Wang, X., and Chopra, I., "Wind Tunnel Test on a slowed Mach-Scaled Hingeless Rotor with Lift Compounding," *Journal of the American Helicopter Society*, Vol. 66, (4), October 2021, pp. 1–17. DOI: 10.4050/JAHS.66.042005.

32. Uppoor, V., Patil, M., and Chopra, I., "Wind Tunnel Testing of a Slowed Mach-scaled Hingeless Rotor with Lift and Thrust Compounding," Vertical Flight Society's 6th Decennial Aeromechanics Specialists' Conference, Santa Clara, CA, February 6–8, 2024.

33. Uppoor, V., Patil, M., and Chopra, I., "Aeromechanics Investigation of Dual-Wing Lift Compounded Slowed Mach-scaled Rotor," Proceedings of the Vertical Flight Society International 80th Annual Forum & Technology Display, May 7-9, 2024.

34. Maurya, S., Chopra, I., and Datta, A., "In Search of Extreme Limits of a Compound Helicopter in High Speed Flight," Proceedings of the Vertical Flight Society International 77th Annual Forum & Technology Display, Virtual, May 10–14, 2021.

35. Hodges, D. H., and Dowell, E. H., "Nonlinear equations of motion for the elastic bending and torsion of twisted nonuniform rotor blades," NASA Technical Note NASA-TN-D-7818, December 1974.

36. Lee, B., and Baeder, J., "Prediction and validation of laminar turbulent transition using SA transition model," AIAA Scitech 2021 Forum, Virtual, January 4, 2021.

37. Leishman, J. G., "Validation of Approximate Indicial Aerodynamic Functions for Two-Dimensional Subsonic Flow," *Journal of Aircraft*, Vol. 25, (10), October 1988, pp. 914–922. DOI: 10.2514/3.45680.

38. Shastry, A., and Datta, A., "Predicting Wake and Structural Loads in RPM Controlled Multirotor Aircraft," Vertical Flight Society's Transformative Vertical Flight 2020 Technical Meeting, San Jose, CA, January 21–23, 2020.

39. Leishman, J. G., and Beddoes, T. S., "A Semi-Empirical Model for Dynamic Stall," *Journal of the American Helicopter Society*, Vol. 34, (3), July 1989, pp. 2–17. DOI: 10.4050/JAHS.34.3.3.

40. Weissinger, J., "The Lift Distribution of Swept-back Wings," NACA TM 1120, March 1947.

41. Jung, Y. S., and Baeder, J., "$\gamma Re\theta t^{-}$ Spalart–Allmaras with Crossflow Transition Model Using Hamiltonian–Strand Approach," *Journal of Aircraft*, Vol. 56, (3), 2019, pp. 1040–1055. DOI: 10.2514/1.C035149.

42. Schubauer, G., and Dryden, H., "The Effect of Turbulence on the Drag of Flat Plates," NACA Technical Report NACA-TR-546, January 1937.